Cell

Structural Basis for dsRNA Recognition, Filament Formation, and Antiviral Signal Activation by MDA5

Bin Wu,[1,3] Alys Peisley,[1,3] Claire Richards,[3] Hui Yao,[4] Xiaohui Zeng,[5] Cecilie Lin,[2] Feixia Chu,[5] Thomas Walz,[2,6] and Sun Hur[1,3,*]

[1]Department of Biological Chemistry and Molecular Pharmacology
[2]Department of Cell Biology
Harvard Medical School, Boston, MA 02115, USA
[3]Program in Cellular and Molecular Medicine, Children's Hospital, Boston, MA 02115, USA
[4]Department of Biochemistry and Molecular Biology, Nankai University, Tianjin 300071, China
[5]Department of Molecular, Cellular & Biomedical Sciences, University of New Hampshire, Durham, NH 03824, USA
[6]Howard Hughes Medical Institute
*Correspondence: hur@idi.harvard.edu
http://dx.doi.org/10.1016/j.cell.2012.11.048

SUMMARY

MDA5, a viral double-stranded RNA (dsRNA) receptor, shares sequence similarity and signaling pathways with RIG-I yet plays essential functions in antiviral immunity through distinct specificity for viral RNA. Revealing the molecular basis for the functional divergence, we report here the crystal structure of MDA5 bound to dsRNA, which shows how, using the same domain architecture, MDA5 recognizes the internal duplex structure, whereas RIG-I recognizes the terminus of dsRNA. We further show that MDA5 uses direct protein-protein contacts to stack along dsRNA in a head-to-tail arrangement, and that the signaling domain (tandem CARD), which decorates the outside of the core MDA5 filament, also has an intrinsic propensity to oligomerize into an elongated structure that activates the signaling adaptor, MAVS. These data support a model in which MDA5 uses long dsRNA as a signaling platform to cooperatively assemble the core filament, which in turn promotes stochastic assembly of the tandem CARD oligomers for signaling.

INTRODUCTION

MDA5 and RIG-I are cytoplasmic viral RNA receptors in the vertebrate innate immune system. They share high sequence similarity and a common signaling adaptor, MAVS, that activates interferon (IFN) signaling pathways. Despite these similarities, they play nonredundant functions in antiviral immunity by recognizing largely distinct groups of viruses and viral RNAs. MDA5 detects long-duplex RNAs in the genome of double-stranded RNA (dsRNA) viruses or dsRNA replication intermediates of positive-strand viruses, such as Encephalomyocarditis virus (EMCV) and vesicular stomatitis virus (VSV) (Kato et al., 2011; Triantafilou et al., 2012). By contrast, RIG-I detects the 5′ triphosphate group (5′ppp) and blunt end of short dsRNAs or single-stranded RNA (ssRNA) hairpins often present in a wide range of negative strand viruses, such as influenza A, and some positive- and double-stranded RNA viruses (Baum et al., 2010; Schlee et al., 2009).

MDA5 and RIG-I consist of the N-terminal tandem caspase activation recruitment domains (2CARD) that activate MAVS, the central helicase domain responsible for RNA-dependent ATP hydrolysis, and the C-terminal domain (CTD). Recent crystal structures of RIG-I provided a detailed view of how RIG-I recognizes the dsRNA end and how 2CARD-mediated signaling activity is autoregulated in the absence of viral dsRNA (Jiang et al., 2011; Kowalinski et al., 2011; Luo et al., 2011). These structures, and those of the isolated CTD (Lu et al., 2010; Wang et al., 2010), showed that the RIG-I CTD plays a predominant role in high-affinity binding and selectivity for dsRNA containing the 5′ppp and blunt end (Cui et al., 2008; Takahasi et al., 2008). In contrast to RIG-I, the MDA5 CTD displays dsRNA affinity that is orders of magnitude lower than that of full-length MDA5 (Peisley et al., 2011), suggesting different molecular mechanisms for dsRNA recognition by MDA5 and RIG-I.

How MDA5 utilizes a domain architecture similar to that of RIG-I to effect vastly different RNA selectivity has remained unclear, largely due to the lack of the MDA5:dsRNA complex structure. Previously, we have shown that MDA5 cooperatively assembles into filamentous oligomers along dsRNA, which is important for high-affinity interaction with long dsRNA (Peisley et al., 2011), and that filament formation correlates with the length-dependent signaling activity in cells due to filament end-disassembly triggered by ATP hydrolysis (Peisley et al., 2012). This is distinct from RIG-I, which tightly binds to dsRNA as a monomer and shows little or no cooperativity in dsRNA binding (Peisley et al., 2011). A previous atomic force microscopy study proposed that RIG-I also forms filaments (Binder et al., 2011), but we have not observed such filaments by

electron microscopy (EM) under the same conditions used for MDA5.

Detailed studies of the MDA5 filament architecture have been challenging partly due to the difficulty of crystallizing filamentous proteins and the potential flexibility of 2CARD upon dsRNA binding. In particular, the latter has been a challenge in RIG-I as well as MDA5 as evidenced by the lack of crystal structures of full-length RIG-I bound to dsRNA. Here, we used three approaches to dissect the architecture of the full-length MDA5 filament and dsRNA recognition mechanism. First, we determined the crystal structure of monomeric MDA5 lacking 2CARD in complex with dsRNA, which allowed direct comparison with RIG-I:dsRNA complex structures. Second, we assembled a model of the MDA5 filament with the crystal structure as a building block and distance constraints derived from protein:protein crosslinking experiments. Finally, we incorporated 2CARD into the filament model by extrapolation of the requirement for an oligomeric assembly of 2CARD in signaling.

RESULTS

MDA5 Binds to 12 bp dsRNA with 1:1 Stoichiometry

We attempted crystallization of human MDA5 lacking the 2CARD domain (MDA5ΔN, residues 298–1025) and a further truncation variant, MDA5ΔN', that lacks both an internal loop (residues 645–662) and the C-terminal tail (residues 1018–1025). Crystals were obtained only from MDA5ΔN' in complex with 12 bp dsRNA (5′-AGGGCCGCGGAT-3′) and an ATP analog, 5′-adenyl-β-imidodiphosphate (ADPNP). The $loop_{645–662}$ and the C-terminal tail are not well conserved (Figure S1A available online), and deletion of these residues did not affect RNA-binding affinity or the ATP-hydrolysis activity of MDA5 (Figures S1B–S1D).

The crystals belonged to space group $P2_12_12_1$ and diffracted to 3.56 Å resolution. The structure was determined by molecular replacement and refined to R_{work} = 27.6% and R_{free} = 32.0% (Table S1). Simulated annealing omit maps (Figures S1F, S2A, and S3B) validated domain organization and other features described in this paper. The asymmetric unit contains two ternary complexes of MDA5ΔN':dsRNA:ADPNP with a stoichiometry of 1:1:1. The stoichiometry of MDA5:12 bp dsRNA was further confirmed in solution using Multiangle light scattering (Figure S1E).

MDA5 Forms a Ring around dsRNA: Commonality with RIG-I

The structure of the ternary complex revealed that MDA5ΔN' forms a ring structure around the 12 bp dsRNA, an architecture that resembles RIG-IΔN bound to dsRNA. Several key features that distinguish MDA5 from RIG-I were also observed, but we will first describe the domain organization and ATP-binding mode that are globally shared between MDA5 and RIG-I.

MDA5ΔN' consists of the two RecA-like domains (Hel1 and Hel2), the intervening Hel2i domain, the pincer domain, and the CTD (Figure 1A). In the structure of MDA5ΔN':dsRNA, these domains are arranged in the order of Hel1-Hel2-Hel2i-CTD around dsRNA counterclockwise from the top view, whereas the V-shaped pincer domain wraps around dsRNA clockwise (Figure 1B). In this arrangement, MDA5 interacts with dsRNA using Hel1, Hel2i, Hel2, and CTD, but not the pincer domain (Figure 1C). Most protein residues interact primarily with the RNA phosphate backbone and 2′ hydroxyl groups, consistent with the sequence-independent recognition of dsRNA (Peisley et al., 2011). These interactions are conserved in RIG-I with the exception of the residues in the CTD (to be discussed later).

To examine the importance of individual domains in dsRNA recognition, residues from each of Hel1, Hel2i, Hel2, and CTD were individually mutated into alanine, and the IFN-β reporter assay was used to examine the signaling activities of these mutants in 293T cells. Stimulation of cells with polyinosinic:polycytidylic acid (pIC), a dsRNA analog known to activate MDA5, induced robust IFN-β promoter activity upon ectopic expression of wild-type (WT) MDA5 but not in the empty vector control (Figure 1D), suggesting that the observed IFN-β signaling is mediated by MDA5. Comparison of WT MDA5 and the point mutants identified several residues, at least one residue per domain, that significantly affect the signaling activity of MDA5 in response to pIC (Figure 1D), indicating that all domains are important for efficient dsRNA recognition.

Cocrystallized ADPNP is bound at the cleft between Hel1 and Hel2 in the outer rim of the MDA5 ring structure (Figures 1B and S1F). Superposition of MDA5 with RIG-I bound to dsRNA and ADP•$BeCl_3$, another ATP analog, by aligning the protein backbone showed a good agreement in their ATP-binding modes. Although detailed analysis of the ADPNP:MDA5 interaction is difficult at the current resolution, the triphosphate group of ADPNP, which is buried deep inside the cleft near residues 332–335, could be unambiguously identified (Figure 1E). The face of the adenine base is placed between the side chains of R309 and R337 (Figure S1F), whereas the edges of the base are within contact distance of Q312 and Q307, which, together, could contribute to the specificity of MDA5 for ATP.

MDA5 CTD Binds to the dsRNA Stem, whereas RIG-I CTD Caps the dsRNA End

A major difference between MDA5 and RIG-I was observed in the orientation of the CTD. In the MDA5ΔN':dsRNA structure, the long axis of the CTD is approximately parallel to the axis of dsRNA, which leaves an ~30° gap between Hel1 and the CTD when viewed from the bottom of the ring (Figures 2A and 2B). This C-shaped ring of MDA5 differs from the RIG-I structure, where the CTD is tilted by ~20° toward the dsRNA, which brings the bottom tip of the CTD closer to Hel1 and forms an asymmetrically closed O-ring around dsRNA (Figures 2A and 2B).

Closer inspection of the CTD:dsRNA interactions in MDA5 and RIG-I revealed that the differential orientation of the CTD is accompanied by dsRNA stem binding by MDA5 versus dsRNA end binding by RIG-I. The RIG-I CTD rigidly caps the end of dsRNA using a loop of residues 848–860, which plays an important role in the recognition of 5′ppp and blunt end of dsRNA. By contrast, the equivalent loop (residues 945–958) in MDA5 is disordered, and dsRNA stem recognition is mediated by residues on the flat surface of the CTD (Figure 2C). In the previous structures of the isolated MDA5 CTD without RNA (Li et al., 2009; Takahasi et al., 2009), this loop (CTD loop) adopts a conformation similar to that of RIG-I with or without RNA

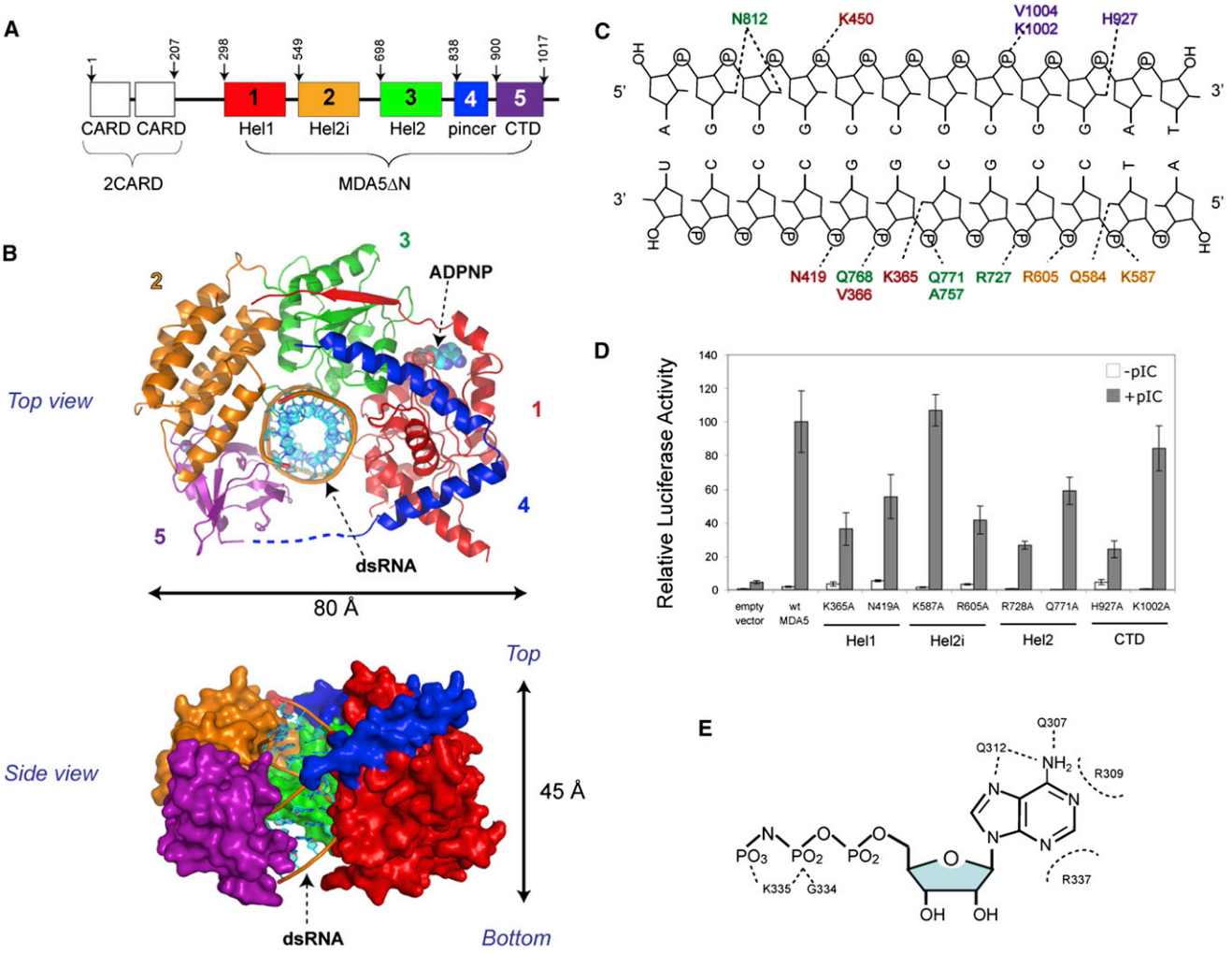

Figure 1. Overview of the Structure of MDA5ΔN':12 bp dsRNA:ADPNP

(A) Schematic of domain organization of human MDA5 with domain boundaries marked by residue numbers.

(B) Top and side views of the ternary complex of MDA5ΔN':12 bp dsRNA:ADPNP in cartoon and surface representation, respectively. Cocrystallized ADPNP is shown as a sphere model (top view). Individual domains are colored as in (A).

(C) Schematic diagram of the MDA5ΔN':dsRNA interactions. Protein residues are colored as in (A).

(D) IFN-β reporter assays of MDA5 and its point mutants (mean ± standard deviation [SD], n = 3). Dual luciferase activities were measured in 293T cells with and without stimulation with pIC.

(E) Schematic diagram of MDA5ΔN':ADPNP interaction.

See also Figure S1 and Table S1.

(Figure S2B). Superposition of the isolated MDA5 CTD onto the MDA5ΔN':dsRNA structure revealed that dsRNA would occupy the same space as the CTD loop in the RNA-free conformation (Figure S2C), suggesting that displacement of the CTD loop is required for dsRNA binding. Consistent with this interpretation, shortening of the loop by deleting residues 945–955 (ΔCTDloop) did not affect the RNA-binding affinity (Figure 2D) and slightly increased the RNA-dependent ATP-hydrolysis activity (Figure S2D). Interestingly, the CTD loop is conserved among MDA5 homologs (Figure S2E), and the signaling activity of the ΔCTDloop mutant is lower, albeit slightly, than that of WT MDA5 (Figure S2F), suggesting that the CTD loop may play as yet unidentified roles in MDA5 function.

Hel2i Provides a Docking Site for MDA5 CTD to Be Positioned near the dsRNA Stem

Although the orientation of the dsRNA-bound MDA5 CTD is distinct from that of the RIG-I CTD, the conformation of the helicase domain is preserved (Cα root-mean-square deviation [rmsd] of 1.9 Å), which prompted the question of what role the helicase domain plays in the divergent evolution of dsRNA specificities. The structures of MDA5 and RIG-I bound to dsRNA show that the CTDs of both proteins form an extensive, long-range intramolecular interaction with Hel2i with buried surface areas of 521 $Å^2$ and 504 $Å^2$, respectively (Figure 3A). The convex surface of the zinc-binding site in the CTD is complementary to the concave surface of Hel2i (Figure 3B), and both the CTD

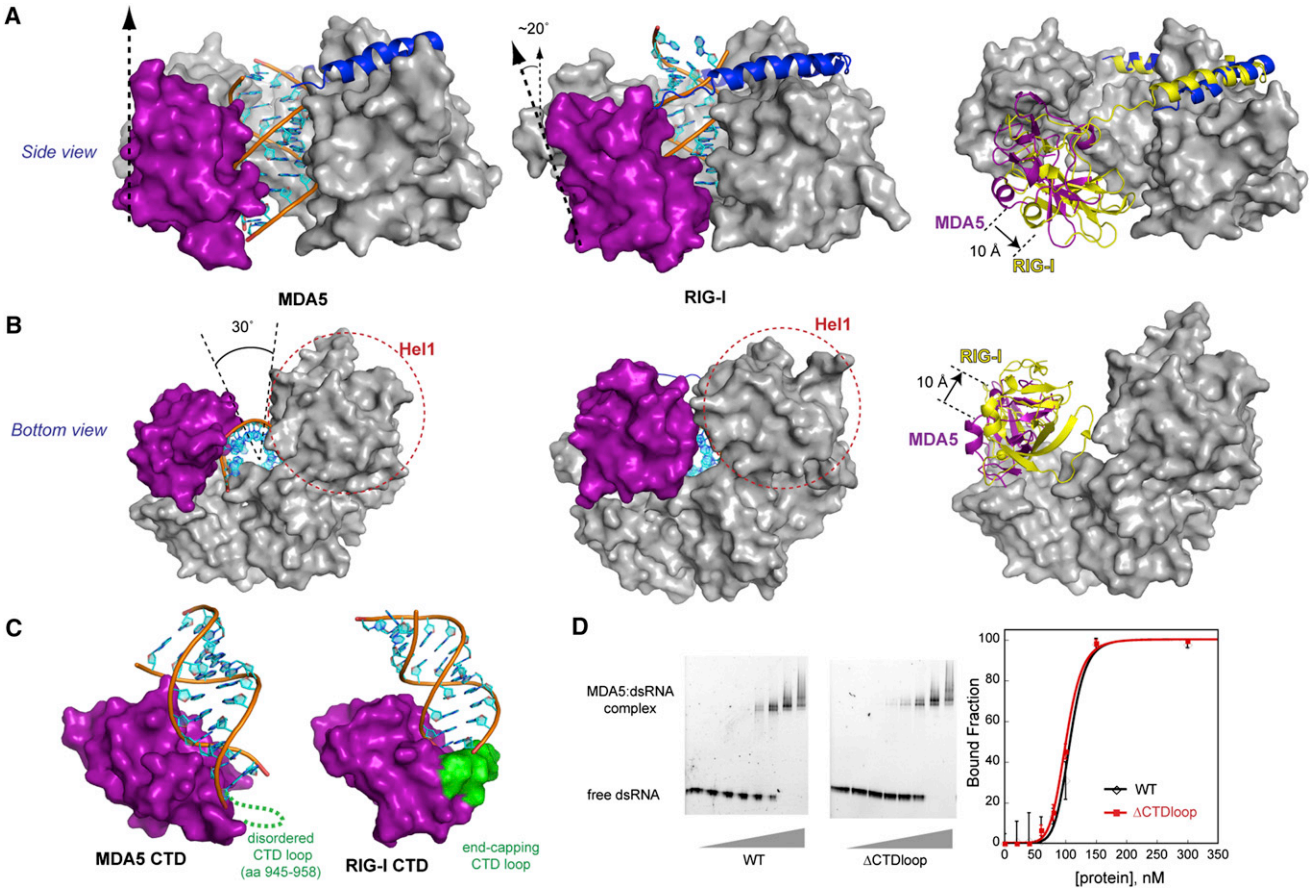

Figure 2. MDA5 Forms an Open Ring Structure around the dsRNA Stem by Orienting the CTD Parallel to the dsRNA Axis

(A and B) Side (A) and bottom (B) views of MDA5ΔN' (left) and RIG-IΔN (right, PDB: 3TMI) bound to dsRNA. The long axis of the CTD (magenta) is indicated by an arrow (side view). On the right, the MDA5 CTD is superposed onto the RIG-I CTD by aligning the helicase domain. RIG-I is colored yellow in the superposed structure.

(C) Comparison of the MDA5 and RIG-I CTDs. The CTD loop in RIG-I (residues 846–859, green, PDB: 3TMI) rigidly caps the dsRNA end, whereas the equivalent loop in MDA5 (residue 945–955) is disordered in the structure of the MDA5ΔN':dsRNA complex.

(D) EMSA of 112 bp dsRNA with WT and the ΔCTDloop mutant of MDA5ΔN (mean ± SD, n = 3).

See also Figure S2.

and Hel2i undergo little conformational change upon complex formation (Figure S3A). We asked whether this rigid-body docking of the CTD against Hel2i plays a role in the differential orientation of the CTD in MDA5 and RIG-I. Superposition of the complex structures of MDA5 and RIG-I by aligning the Hel2i domains showed that the RIG-I CTD is ~10 Å farther removed from Hel2i than the MDA5 CTD (Figure 3C). Notably, helix α12 in RIG-I Hel2i at the interface with the CTD is 10 residues longer than in MDA5 in all species examined (Figure 3D), and the resultant protrusion of helix α12 could push the RIG-I CTD away from Hel2i. Consistent with the importance of the surface complementarity between Hel2i and the CTD, a chimera that contains RIG-I helicase and MDA5 CTD has a significantly lower affinity for dsRNA than full-length MDA5 (Figure 3E). Thus, despite having a similar conformation, the helicase domain of MDA5 is not interchangeable with that of RIG-I, and its role is beyond simply providing additional RNA affinity but likely includes precise positioning of the CTD for efficient recognition of the dsRNA stem.

Hel2 Recognizes the dsRNA Stem by Inserting a Loop into the Major Groove

By comparison to RIG-I, the dsRNA stem-binding mode of MDA5 results in a differential positioning of the dsRNA relative to the helicase domain, in particular the loop in the Hel2 domain (residues 758–767, Hel2 loop). In the MDA5ΔN':dsRNA structure, the Hel2 loop is inserted into the major groove of the dsRNA stem, whereas in RIG-I, it binds to the dsRNA end (Figures 4A and S3B). The major groove, which often serves as a sequence-dependent recognition site for dsDNA-binding proteins, is typically too narrow in dsRNA to accommodate a protein secondary structure. In the MDA5:dsRNA complex, the major groove is widened from 12 Å to 18 Å at the site of Hel2 loop insertion (Figure 4A), but unlike many DNA-binding proteins,

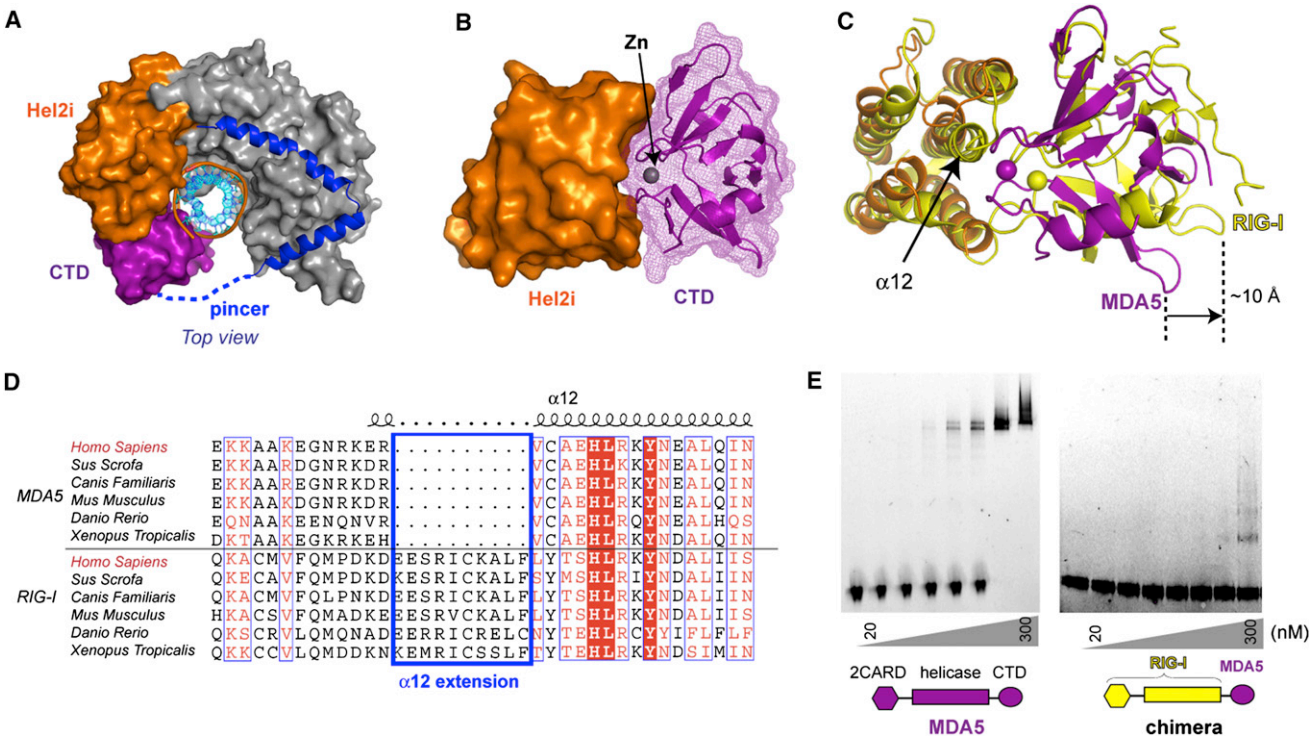

Figure 3. CTD Is Rigidly Held by Hel2i through Surface Complementarity

(A) Top view of the MDA5ΔN':dsRNA complex showing the long-range interaction between Hel2i (orange) and the CTD (purple). Hel1, Hel2 (gray), and Hel2i form one continuous half-ring structure that is connected to the CTD (purple) via the long, partially disordered pincer domain (blue).

(B) Surface representation of Hel2i and the CTD within the MDA5ΔN':dsRNA complex. See also Figure S3A.

(C) Superposition of the structures of Hel2i:CTD of MDA5 (orange:magenta) and RIG-I (yellow:yellow, PDB: 3TMI) by aligning the Hel2i backbone.

(D) Sequence alignment of MDA5 and RIG-I homologs near helix α12 in Hel2i.

(E) EMSA of 112 bp dsRNA with WT MDA5 and a chimera consisting of RIG-I 2CARD-helicase and MDA5 CTD.

the interaction between the inserted loop and dsRNA is limited to the phosphate backbone and does not lead to a sequence-dependent base recognition.

To examine the importance of the Hel2 loop in dsRNA recognition, we engineered MDA5ΔN lacking the Hel2 loop (ΔHel2loop) and tested its ability to bind dsRNA and hydrolyze ATP. Interestingly, ΔHel2loop did not affect dsRNA affinity (Figure 4B) but completely abolished the dsRNA-dependent ATP-hydrolysis activity (Figure 4C), which was unexpected based on ΔHel2loop's distant location from the ATP-binding site (Figure 4D). In the cell, ΔHel2loop led to a complete loss of signaling activity (Figure 4E), consistent with the previous proposal that ATP hydrolysis is important for signal activation (Yoneyama et al., 2005). These observations suggest that insertion of the Hel2 loop into the major groove is important not for RNA binding but for ATP hydrolysis and subsequent signaling and could potentially serve as an additional mechanism to discriminate between dsRNA and other types of nucleic acids.

Monomers in MDA5 Filaments along dsRNA Are Arranged Head-to-Tail

We next asked how the MDA5 ring stacks along dsRNA to form the filamentous oligomers that we observed in our previous EM studies (Peisley et al., 2011). The packing of the individual MDA5 molecules in our crystal does not recapitulate the continuous filament architecture, possibly reflecting incompatibility between the filament geometry and the crystal packing. The crystal structure enabled us, however, to build filament models by joining MDA5 monomers either in a head-to-tail or head-to-head/tail-to-tail arrangement (Figure 5A). We used two constraints in building the models, namely preserving the helical symmetry of dsRNA at the monomer:monomer interface and avoiding a severe clash and gap between the adjacent monomers. The resultant head-to-tail model shows a repeating unit of ~14 bp and a turn of ~70° per monomer, which places helix α10 (in the head surface of monomer 1) right below α18 (in the tail surface of monomer 2) (Figure 5A). In the head-to-head and tail-to-tail models, the two adjacent monomers are related by a two-fold symmetry, and helix α18 of monomer 1 is placed next to another α18 of monomer 2 but away from α10 (Figure 5A).

To distinguish between the head-to-tail and head-to-head/tail-to-tail models, we employed a Cys-based protein-protein crosslinking (X-linking) strategy to take advantage of the fact that MDA5ΔN' contains only four surface-exposed Cys's. To identify residues proximal to α10, we first mutated the four native Cys's to Ala's and engineered a new Cys at position 556, 559, or 563 within the helix α10 and at position 860 within the head surface but outside the putative interface as a negative control.

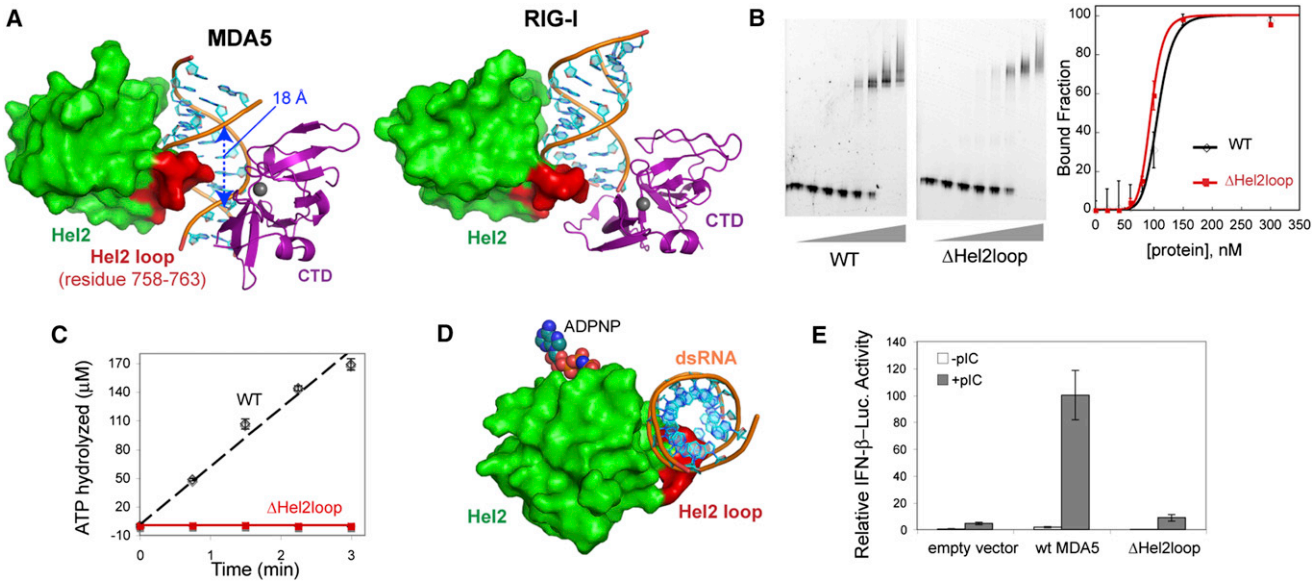

Figure 4. The Hel2 Loop Is Inserted into the Major Groove of dsRNA

(A) Position of the Hel2 loop (red) relative to dsRNA in MDA5 (left) and RIG-I (right, 3TMI). The Hel2 loop of MDA5 is inserted into the major groove, which is accompanied by widening of the major groove from 12 Å to 18 Å, whereas the RIG-I loop is near the dsRNA end with little change in the width of the major groove. See also Figure S3B.

(B) EMSA of 112 bp dsRNA with WT MDA5ΔN and the ΔHel2loop mutant (mean ± SD, n = 3).

(C) Time course of ATP hydrolysis by WT MDA5ΔN and the ΔHel2loop mutant (mean ± SD, n = 3).

(D) Top view of MDA5 Hel2 with dsRNA and ADPNP.

(E) IFN-β reporter assays of WT and ΔHel2loop of full-length MDA5 (mean ± SD, n = 3).

These four sites are equally solvent accessible in the structure of the MDA5ΔN' monomer, and their Cys mutants bind to dsRNA and form filaments as efficiently as WT MDA5 (Figures S4A–S4C). We first examined whether these Cys mutants can be X-linked with bis-maleimidoethane (BMOE), which is known to introduce Cys-Cys, and to some extent, Cys-Lys X-links at pH 7.5, the reaction condition used in our assays. We compared the X-linking efficiency of the mutants when bound to 112 bp or 15 bp dsRNA, which accommodates eight or single MDA5 monomers, respectively. Incubation of the C559 mutant with 112 bp dsRNA, but not with 15 bp or without RNA, led to extensive intermolecular X-linking that displayed a ladder pattern in SDS-PAGE (Figure 5B). This differs from intramolecular X-links (migrating near the uncrosslinked protein), which were present in all samples independent of RNA. The 112 bp-mediated intermolecular X-linking was also highly dependent on the position of the Cys; C563 displayed a less extensive ladder pattern than C559, whereas C556 and C860 showed little or no ladder formation (Figure 5B). To examine the possibility of 112 bp dsRNA inducing nonspecific bridging of MDA5 monomers as opposed to cooperative filament formation, we compared the X-linking efficiency in the presence of 2- to 5-fold excess of 112 bp dsRNA over protein to selectively suppress a nonspecific bridging effect. No difference was observed in either the X-linking pattern or efficiency (Figure S4D), suggesting that intermolecular X-linking is due to specific filament formation.

To identify the X-linking partner of C559, we performed liquid chromatography-mass spectrometry (LC-MS) and liquid chromatography-tandem mass spectrometry (LC-MS/MS) analyses on the in-gel tryptic digests of the 112 bp-specific X-linked products. We compared inter- and intramolecular X-links to unambiguously identify intermolecularly X-linked peptides. The most prominent peptide from intermolecular but not intramolecular X-link digest was detected at mass-to-charge ratio (*m/z*) 671.02^{3+} (Figure 5C). This peptide was subject to cleavage in MS/MS analysis, which indicated K777 as the X-link partner of C559 (Figure 5D). To confirm this result, we also used sulfo-MBS, a more commonly used Cys-Lys X-linker, and identified the same C559-K777 pair as the most prominent X-link that is present only in the intermolecularly but not in the intramolecularly X-linked species (Figures S4E–S4G).

These results show that, in the filament, K777 from helix α18 is in close proximity to C559 from helix α10, which is compatible with the head-to-tail but not the head-to-head or tail-to-tail model. Furthermore, the high sensitivity of X-linking to the Cys position imposes strong geometry constraints that specifically support the filament model with an interval of 14 bp but not 13 bp or 15 bp. In the model with a 14 bp interval, the Cβ atom of K777 is at a distance of 17, 12, or 15 Å from the Cβ atoms of C556, C559, or C563, respectively (Figure 5E). Considering the length of Lys and Cys side chains (~4–5 Å between Cβ and Nζ in Lys and 1.8 Å between Cβ and Sγ in Cys) and the arm length of BMOE (8 Å), C559 and potentially C563, but not C556, can be within the X-link distance limit. In the head-to-tail models with 13 bp and 15 bp intervals, the distance between Cβ's of K777 and C559 (>16 Å) are beyond the BMOE X-linking

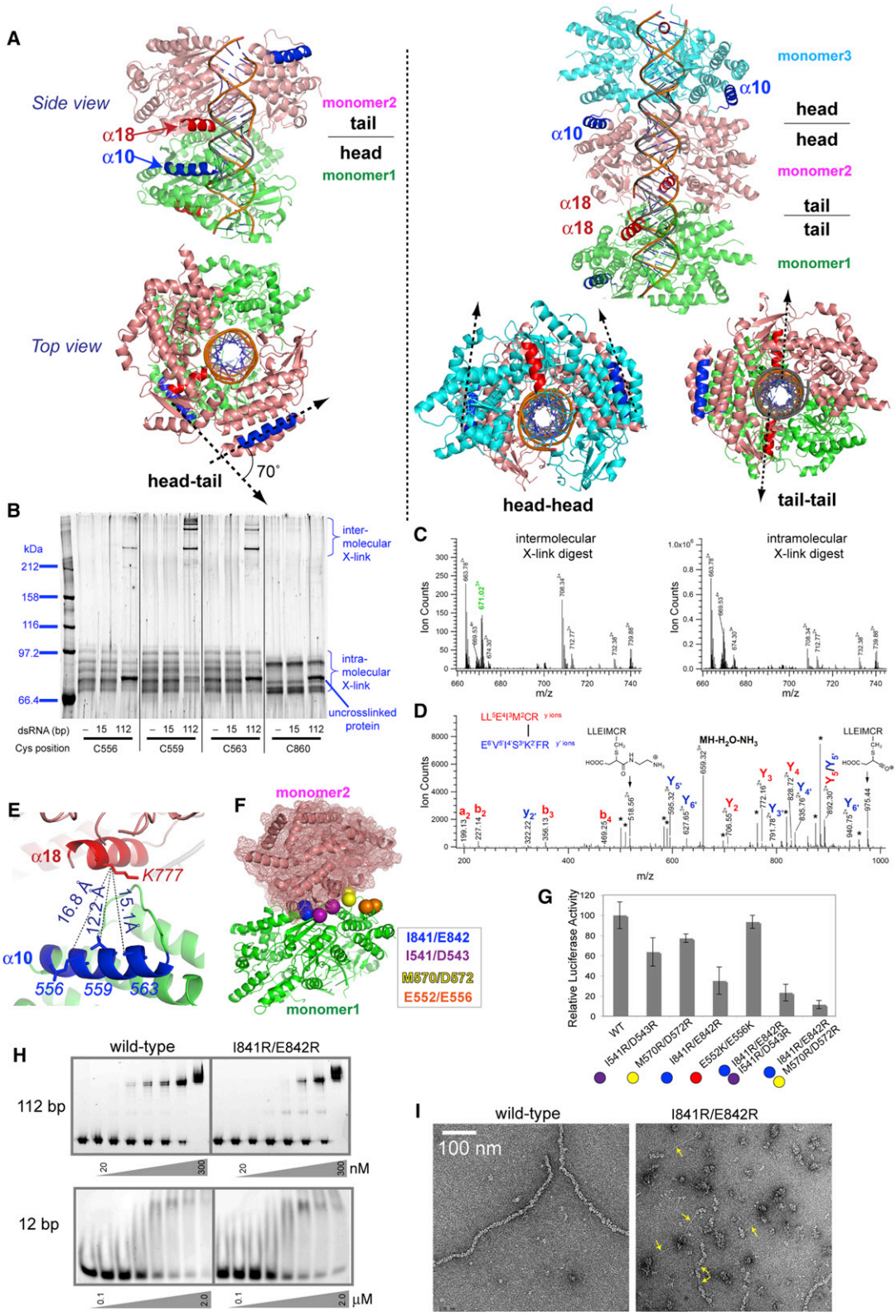

Figure 5. MDA5 Forms a Head-to-Tail Filament In Vitro and In Vivo

(A) Side and top views of head-to-tail and head-to-head/tail-to-tail models of the MDA5ΔN' filament; models were built based on the structure of the MDA5ΔN':dsRNA complex. Bridging RNA (gray) was added to join monomers while preserving dsRNA continuity.

(legend continued on next page)

limit, and there are significant levels of steric clash and gap between the adjacent monomers, respectively. This model predicts pseudo-five-fold symmetry (~70° turn per monomer) within a filament, which is in agreement with the recent EM analysis of the mouse MDA5 filament (Berke et al., 2012).

We used the head-to-tail model with an interval of 14 bp to predict the monomer:monomer interface with the total buried surface area of ~1,500 Å^2, which largely involves interaction between the helicase and helicase or pincer domains. To examine this filament model in the cell, we designed three pairs of mutations, I541R/E543R, M570R/E572R, and I841R/E842R, on the head surface at the putative interface and one pair of control mutations, E552K/E556K, on the head surface just outside the interface (Figure 5F). These residues, which are conserved in MDA5 but not in RIG-I (Figure S4H), are not in contact distance from dsRNA in our structure. The three pairs of mutations at the putative interface showed a range of negative and additive impact on the signaling activity of MDA5 as measured by IFN-β reporter assays, whereas the control mutation did not (Figure 5G). Of note, the least active mutant, I841R/E842R, displayed reduced affinity for 112 bp dsRNA while retaining the WT affinity for 15 bp dsRNA. As affinity for long dsRNA reflects both protein monomer:RNA and monomer:monomer interactions within the filament, whereas affinity for 15 bp dsRNA reflects the intrinsic monomer:RNA interaction, these results suggest that the mutation specifically disrupts the monomer:monomer interaction within the filament (Figure 5H). Consistent with this notion, EM analysis showed that I841R/E842R forms short fragments of filaments dispersed along 1012 bp RNA (Figure 5I). Altogether, these observations support formation of the head-to-tail MDA5 filament in the cell and its importance for signaling.

Isolated MDA5 2CARD Forms Elongated Oligomers

In pursuit of understanding the architecture of a filament formed by full-length MDA5 and the mechanism for signal activation, we asked how the signaling domain, 2CARD, which is absent in our crystal structure or in the filament model, is arranged within the MDA5 filament. In our previous EM analysis, class-averaged projection images of the MDA5 filament only showed a ring structure and lacked any density that could correspond to 2CARD (Peisley et al., 2011). This observation suggests that 2CARD does not constitute the core filament architecture and is flexible. The linker between 2CARD and the helicase domain is ~100 amino acids long and is predicted to be largely disordered (Figure S5A). Comparison between MDA5 and MDA5ΔN filaments showed little difference in filament morphology (Figure 6A). To better locate 2CARD with respect to the core filament, we fused a 60 kDa *E. coli* protein, NusA, to the N terminus of MDA5. NusA-MDA5 assembled into thicker filaments than MDA5ΔN (width of 12–18 nm in comparison to ~9 nm) and displayed a more rugged filament surface with irregular bulges appearing along the filament (Figure 6A). This observation suggests that NusA-2CARD decorates the outer surface of the MDA5 core filament with a high degree of heterogeneity.

Self-oligomerization is a common molecular property of many members of the death domain superfamily (Ferrao and Wu, 2012), which 2CARD belongs to, and can often be reconstituted by overexpression. We overexpressed isolated 2CARD in *E. coli* and analyzed the purified protein by size-exclusion chromatography (SEC). We found that ~30%–40% of 2CARD existed in high-molecular-weight species (HMW) and ~40%–50% in low-molecular-weight species (LMW) (Figure 6B). This is different from RIG-I 2CARD, which expressed predominantly as a monomer (Figure S5B). Purified HMW and LMW of MDA5 2CARD were stable with no apparent change in size over ~6 hr, but HMW gradually broke down into smaller pieces upon dilution, and LMW converted to HMW upon concentration, suggesting their concentration sensitivity. Under EM, the HMW species displayed heterogeneous, elongated oligomeric architectures that were ~20–60 nm long and ~13 nm wide (Figure 6C). The structure of MDA5 2CARD is unknown, but based on the size of RIG-I 2CARD (5 nm long and 2.5 nm wide) in the crystal structure of full-length RIG-I (Kowalinski et al., 2011), we suspect that the HMW of MDA5 2CARD consists of multiple 2CARD molecules in both width and length. Despite the heterogeneity, such an elongated shape is distinct from dysfunctional protein aggregates that usually display a round or amorphous shape, as was seen with loss-of-function mutant G74A/W75A 2CARD (Figure 6C) (Jiang et al., 2012). This result suggests that the observed elongated shape of WT 2CARD HMW reflects an intrinsic propensity of 2CARD to self-assemble into a defined oligomeric arrangement.

(B) Krypton stain of an SDS gel of BMOE-X-linked MDA5ΔN' variants containing Cys at positions 556, 559, 563, or 860. The proteins were preincubated with 15 bp or 112 bp dsRNA prior to X-linking with BMOE.

(C) Mass spectrometric analysis of inter- versus intramolecular X-link of the C559 mutant. The BMOE-X-linked bands were in-gel digested, excised as indicated in (B), and subjected to mass spectrometry, which identified a peptide of *m/z* 671.02^{3+} that was only present in the inter- but not intramolecularly X-linked sample.

(D) Tandem mass spectrum of the peptide (*m/z* 671.02^{3+}) from (C). C terminus containing fragment ions y and y' indicates that C559 is X-linked to K777. * indicates fragment ions from neutral loss.

(E) Magnified view of the α10 (head) -α18 (tail) interface from the head-to-tail model in (A). Distances were measured between Cβ's of K777 and C556, C559, or C563.

(F) Location of residues mutated in (G) (spheres). I541/E543, M570/E572, and I841/E842 are on the head surface at the putative interface, whereas E552/E556 are just outside the interface.

(G) IFN-β reporter assays of WT MDA5 and mutants (residues shown in F) upon pIC stimulation (mean ± SD, n = 5).

(H) EMSA of WT and I841/E842 mutant MDA5ΔN with 112 bp or 15 bp dsRNA.

(I) Representative EM images of WT and I841R/E842R mutant MDA5ΔN (0.3 μM) bound to 1012 bp dsRNA (2.4 μg/ml). Long stretches of naked dsRNA exposed in the mutant complex are indicated by arrows.

See also Figure S4.

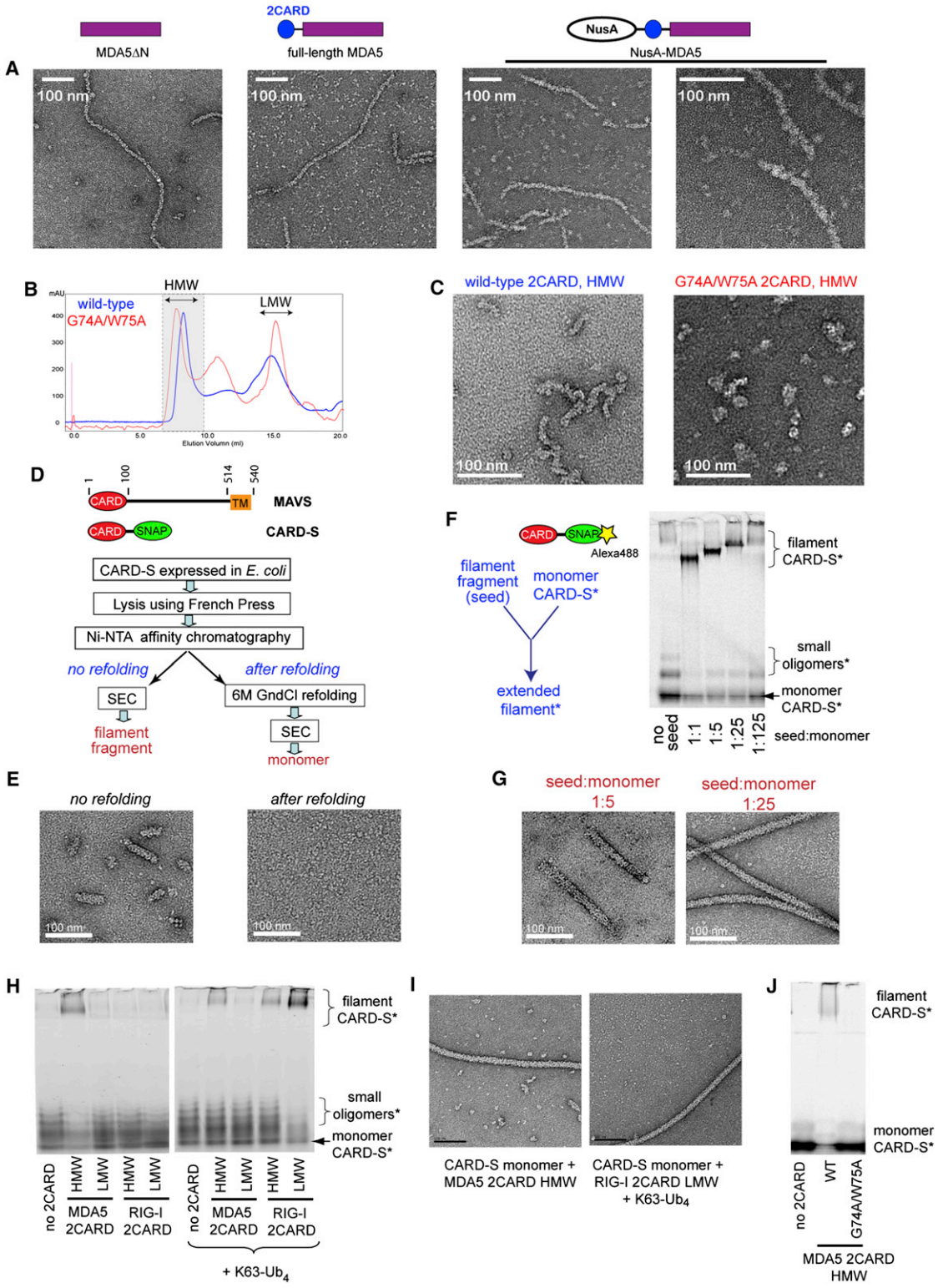

Figure 6. MDA5 2CARD Forms Functional Oligomers

(A) Electron micrographs of filaments formed by MDA5ΔN, MDA5, and NusA-MDA5 with 1,012 bp dsRNA.

(B) Overlaid SECs (Superdex200 10/300) of purified isolated 2CARD of WT MDA5 and the G74A/W75A mutant.

(C) Electron micrographs of HMW species of 2CARD of WT MDA5 and the G74A/W75A mutant.

(D) Schematic of domain organization and purification procedure of MAVS CARD-S with and without refolding.

(legend continued on next page)

MDA5 2CARD Oligomers, but Not Monomers, Promote MAVS Filament Formation

To examine the significance of the oligomerization of MDA5 2CARD, we developed biochemical assays to monitor the effect of HMW of MDA5 2CARD on the activation of the signaling adaptor MAVS. Previous studies showed that MDA5 and RIG-I 2CARD activate MAVS by promoting formation of prion-like filaments consisting of the N-terminal CARD of MAVS (Hou et al., 2011). To examine the impact of MDA5 2CARD on formation of MAVS CARD filaments, we expressed and purified recombinant MAVS CARD fused to a SNAP tag (18 kDa) (Figure 6D), which increased solubility of the protein and allowed fluorescent labeling for monitoring formation of MAVS filaments. MAVS CARD fused to SNAP (CARD-S), but not SNAP alone, expressed as short (~30–100 nm) fragments of filaments (Figure 6E), which resemble the filament of MAVS CARD purified from mammalian cells (Hou et al., 2011). To examine the prion-like property for the CARD-S filament, we performed a seeding experiment by mixing CARD-S filament seeds with monomeric CARD-S. We prepared monomeric CARD-S by chemical denaturation of CARD-S filaments followed by refolding and SEC in native buffer (Figure 6D). This procedure produced a monomeric CARD-S that is stable for at least ~24 hr before it spontaneously forms filaments over the course of 3–7 days. To distinguish between the seed filaments and monomeric CARD-S, we labeled monomeric CARD-S with Alexa 488 (CARD-S*, * indicates fluorescent labeling). When monomeric CARD-S* was mixed with unlabeled seed filaments, CARD-S* was rapidly incorporated into the filament within 30 min as evidenced by EM and the mobility shift in the native gel (Figures 6F, 6G, and S5E). In addition, the lengths of the resultant filaments were inversely related to the added amount of seed filaments (Figures 6F and 6G), a growth characteristic similar to prions.

We next examined whether monomeric CARD-S* can form filaments de novo (in the absence of seed filaments) in response to RIG-I and MDA5 2CARD. Previous studies showed that RIG-I 2CARD can promote formation of MAVS filaments on mitochondria upon addition of free chain of K63-linked tetraubiquitin (K63-Ub_4) (Hou et al., 2011). Using purified, monomeric CARD-S*, we also observed that the combination of RIG-I 2CARD and K63-Ub_4 but not K48-Ub_4 or linear Ub_4 induced a mobility shift of CARD-S* in a native gel (Figures 6H and S5F) and formed filaments as seen by EM (Figure 6I). Both LMW and HMW of RIG-I 2CARD stimulated CARD-S* filament formation with LMW being more effective (Figure 6H). These results suggest that RIG-I-mediated MAVS activation can be reconstituted with purified, soluble MAVS CARD.

Next, we incubated CARD-S* with MDA5 2CARD. Unlike RIG-I, we did not observe any stimulatory effect of K63-Ub_4 on MDA5 2CARD in inducing CARD-S* filament formation (Figure 6H). However, HMW, but not LMW, of MDA5 2CARD was able to induce a mobility shift of CARD-S* in EMSA and filament formation by EM (Figures 6H–6J). HMW of the loss-of-function mutant G74A/W75A did not stimulate CARD-S* filament formation (Figures 6H–6J). In addition, filament formed by MDA5 2CARD HMW displayed prion-like properties as it rapidly incorporated monomeric CARD-S labeled with Alexa 647 into the filament (Figure S5G). These results suggest the importance of 2CARD oligomerization for MAVS activation.

2CARD Oligomerization in the Full-Length MDA5 Filament

The requirement of 2CARD oligomerization for signaling suggests that 2CARD must oligomerize within the MDA5 filament to activate MAVS. The structure of full-length RIG-I revealed that 2CARD is masked by an intramolecular interaction in the absence of dsRNA but becomes exposed upon dsRNA binding (Kowalinski et al., 2011). Assuming a similar scenario for MDA5, one might expect that release of 2CARD upon dsRNA binding could be sufficient for 2CARD oligomerization. However, we found that MDA5 bound to 15 bp dsRNA is monomeric (Figure S6A), suggesting that exposure of 2CARD is insufficient to induce its oligomerization. This result is consistent with our observation that isolated 2CARD does not spontaneously oligomerize until it is highly concentrated.

We next asked what factors besides dsRNA binding would be required for oligomerization of 2CARD in full-length MDA5. Filament formation could bring multiple 2CARDs into proximity and could promote oligomerization. However, our and others' observations that catalytic mutants are impaired in signaling (Figures 4E and S6B) (Yoneyama et al., 2005) prompted us to examine how ATP hydrolysis regulates signaling, in particular the conformation of 2CARD. We employed a protease-protection assay with N-terminally labeled MDA5 to monitor proteolysis of 2CARD. As ATP hydrolysis induces repetitive cycles of filament assembly and disassembly (Berke and Modis, 2012; Peisley et al., 2011), which would complicate the analysis, we used several nonhydrolyzable analogs mimicking ATP at various stages of hydrolysis to probe conformational rearrangement during ATP hydrolysis. We found protection of 2CARD against chymotrypsin, trypsin, and proteinase K in the presence of

(E) EMs of CARD-S with and without refolding.
(F) CARD-S filament extension assay. Unlabeled seed filaments of CARD-S were incubated with Alexa 488-labeled, monomeric CARD-S (CARD-S*, * indicates Alexa 488 label, 10 μM) at the indicated mass ratios for 30 min at RT prior to gel analysis. Shown is an Alexa 488 fluorescence gel image to specifically monitor CARD-S* transitioning from the monomeric to the filamentous state.
(G) EMs of the extended filaments of CARD-S from (F).
(H) CARD-S filament formation assay. Alexa 488-labeled, monomeric CARD-S* (10 μM) was incubated with HMW or LMW of MDA5/RIG-I 2CARD (10 μM) with and without K63-Ub_4 (2.5 μM) for 2 hr at RT prior to gel analysis. Shown is an Alexa 488 fluorescence gel image.
(I) EMs of a CARD-S filament induced by MDA5 2CARD (HMW) alone or RIG-I 2CARD (LMW) and K63-Ub_4. Experiments were performed as in (H).
(J) Comparison of CARD-S filament formation in the presence and absence of HMW 2CARD of WT MDA5 and the G74A/W75A mutant. Experiments were performed as in (H).
See also Figure S5.

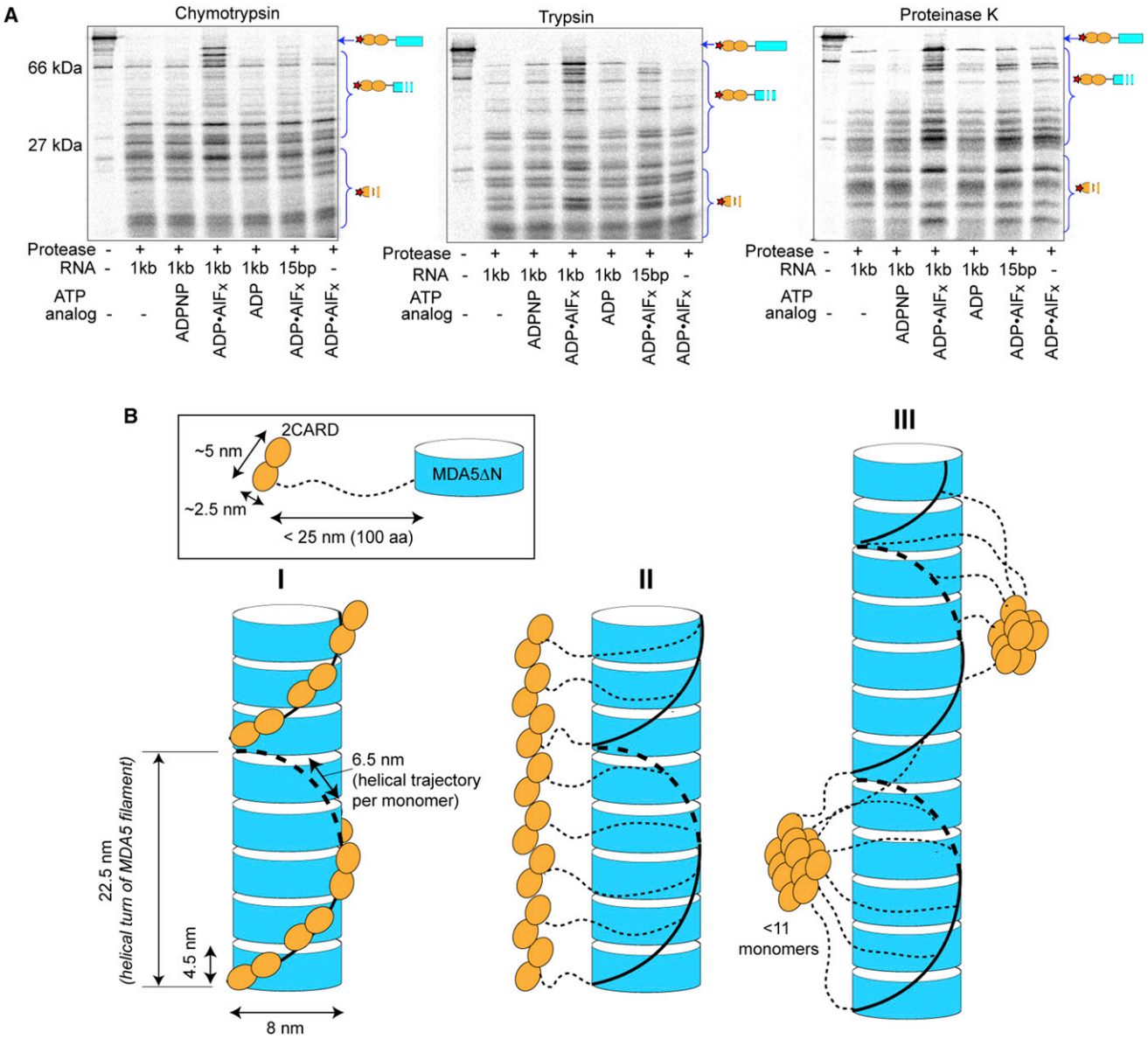

Figure 7. Oligomerization of 2CARD in the Full-Length MDA5 Filament

(A) Protease-protection assay. MDA5 with the N-terminal fluorescein label (star) was incubated with or without 15 bp or 1,012 bp dsRNA, and ADPNP, ADP•AlF_x, or ADP, and subjected to limited-proteolysis by chymotrypsin, trypsin, or proteinase K prior to analysis by SDS-PAGE. See Extended Experimental Procedures for details.

(B) Models of the full-length MDA5 filament. In the first two models, 2CARD forms a continuous filament along the helical trajectory of the MDA5 core filament or alongside the core filament. Alternatively, 2CARD forms discrete patches of oligomers along the filament with heterogeneous size distributions. Inset: geometry constrains used in the model. The size of 2CARD was predicted based on the structure of RIG-I 2CARD (Kowalinski et al., 2011). The maximum linker length, 25 nm, was calculated based on the secondary structure prediction (Figure S5A) and the assumption that each residue contributes an increment of 1.5 Å and ~3 Å within an α helix and a random coil, respectively.

See also Figure S6.

ADP•AlF_x (transition state or post-hydrolysis mimic) in comparison to ADPNP (ground-state mimic), ADP (product after phosphate release), or without ligand (Figure 7A). This protection was more effective when MDA5 was bound to long (1,012 bp) dsRNA than with or without 15 bp dsRNA (Figure 7A). No such dependence on the ATP analog was observed with the catalytic mutant K335A (Figure S6C). These results support the notion that ATP hydrolysis regulates the conformation of 2CARD, and more protection of 2CARD in long dsRNA is consistent with its oligomerization within the filament.

We next modeled 2CARD into the head-to-tail filament architecture of MDA5. We examined three models based on the

geometry constraints derived from the helical symmetry of the MDA5 filament (Figure 5A), the size of 2CARD (based on RIG-I 2CARD structure), and the predicted length of the linker between 2CARD and the helicase domain (<25 nm). In the first two models (Figures 7B, panels I and II), we examined whether it is possible for 2CARD to form a continuous filament along or alongside the MDA5 core filament. Calculation of the helical trajectory suggests, however, that 2CARD cannot form a continuous filament along the helical trajectory because it is ~30% longer than the maximum length that 2CARD can cover (Figure 7B, panel I). Alternatively, a 2CARD filament could run alongside the core MDA5 filament as the linker is long enough to wrap half around the core filament (Figure 7B, panel II). In this model, 2CARD would need to be stacked linearly as the rise of the MDA5 core filament (4.5 nm) is only slightly shorter than 2CARD. This linear arrangement, however, is incompatible with the intrinsic preference of the isolated 2CARD (or other death domains; Ferrao and Wu, 2012) to oligomerize in both width and length (Figure 6C). Thus, we propose a model in which 2CARD forms discrete patches of oligomers along the filament (Figure 7B, panel III), where each patch resembles the local structure of the 2CARD oligomer observed with isolated 2CARD (Figure 6C). In this model, size, frequency, and positioning of individual patches are stochastically determined during MDA5 filament assembly and ATP hydrolysis with an upper size limit of ~11 monomers per patch (number of monomers within the maximum length of two linkers, 50 nm). The stochastic nature of 2CARD clusters rationalizes heterogeneity of NusA-2CARD bulges observed with the NusA-MDA5 filament (Figure 6A).

DISCUSSION

The vertebrate innate immune system utilizes pattern recognition receptors to detect a variety of molecular signatures from a broad range of pathogens. Underlying this functional diversity is a surprisingly small number of structurally distinct domains that include the DExH box helicase domain in RIG-I and MDA5 and leucine-rich repeats in Toll-like receptors and Nod-like receptors (Palsson-McDermott and O'Neill, 2007). How these receptors utilize similar domain architectures to recognize vastly different ligands and acquire a unique biological function is a key recurring question. In order to understand the structural mechanism for the divergent viral RNA recognition by RIG-I and MDA5, we here provided unprecedented details of the molecular architecture of MDA5, which has thus far lagged behind our understanding of RIG-I. We used three approaches: first, we determined the crystal structure of the MDA5ΔN' monomer bound to dsRNA; second, we modeled the MDA5 core filament based on the crystal structure and geometry constraints from protein X-linking experiments; and finally, we added 2CARD into the model of the MDA5 core filament based on our observation that 2CARD must oligomerize in order to activate MAVS.

The crystal structure of MDA5ΔN':dsRNA demonstrates that MDA5 binds to dsRNA as a monomer with a global domain organization similar to that of RIG-I. However, MDA5 utilizes differential orientation of the CTD, which is 20° rotated compared with the RIG-I CTD, to recognize the internal duplex structure of dsRNA. This slight difference in CTD orientation results in an open, C-ring-shaped structure of MDA5 that binds to the dsRNA stem, as opposed to the O-ring structure that is formed by RIG-I and caps the dsRNA end (Figures 2A and 2B). In addition, differential flexibility of a loop in the CTD (residues 945–955) also appears to contribute to the divergent RNA selectivity of MDA5 and RIG-I. In RIG-I, this loop rigidly caps the end of dsRNA, whereas in MDA5, it is displaced from the core CTD structure as it competes with dsRNA for the same surface of the CTD core (Figure S2C). The MDA5 helicase domain also contributes to the dsRNA stem recognition despite sharing similar conformation with RIG-I. The Hel2i domain provides a docking site for the CTD to be rigidly held near the dsRNA stem (Figure 3), and the Hel2 loop inserts into the major groove, serving as a key checkpoint in dsRNA-dependent ATP hydrolysis and signaling (Figure 4). Thus, close collaboration between the helicase domain and the CTD provides the molecular basis for the divergent RNA specificity of MDA5 and RIG-I.

Could this stem-binding mode occur with RIG-I? Although the dsRNA end appears to be the primary site of recognition by RIG-I, accumulating evidence suggests that RIG-I can also recognize the dsRNA stem. Previous studies showed that RIG-I-mediated signaling increases with dsRNA length at a constant molar amount (i.e., constant amount of the dsRNA end but increasing amount of stem), suggesting a positive role of the dsRNA stem in activating RIG-I (Binder et al., 2011). In addition, single-molecule analysis revealed that RIG-I translocates during ATP hydrolysis, which inevitably requires at least transient interaction between the dsRNA stem and RIG-I (Myong et al., 2009). Binding of RIG-I to the dsRNA stem would require a CTD conformation different from those in the crystal structures of RIG-IΔN:dsRNA. It is tempting to speculate that RIG-I adopts a conformation similar to that of MDA5 for dsRNA stem recognition.

The open ring structure of MDA5, but not the closed ring of RIG-I, is compatible with the filament architecture we observed in our previous EM studies (Peisley et al., 2011). The MDA5 filament is distinct from a "beads-on-a-string" type of oligomer as evidenced by the proximity between the adjacent monomers (within 8 Å X-linking distance), which is unaffected by the presence of an excess amount of RNA (Figure S4D). By identifying the residues involved in X-linking, we demonstrated that filaments are formed by stacking MDA5 monomers in a head-to-tail arrangement with a 70° turn per monomer (Figure 5A). This brings the helicase domain in contact with adjacent helicase domains through an extensive protein:protein contact, which rationalizes the observed high cooperativity of MDA5 in dsRNA binding and its high affinity for long dsRNA far beyond the linear combination of monomer interactions. Mutations at the interface, but not at distal sites, impaired filament formation of MDA5 in vitro and the signaling activity in the cell (Figures 5G–5I), further supporting the filament model and its importance in vivo.

Defining the complete architecture of full-length MDA5 requires knowledge of the arrangement of 2CARD within the filament. With isolated 2CARD as a model system, we found that 2CARD can self-oligomerize into a higher-order structure at high protein concentration, and that this oligomerization is

required for 2CARD to promote MAVS filament formation (Figure 6). Based on this requirement for 2CARD oligomerizaton, and other geometric constraints derived from the MDA5 core filament and the linker connecting between 2CARD and the core filament, we reconstructed a model in which 2CARD forms patches of signaling-competent oligomers along the MDA5 filament (Figure 7B, panel III). RNA binding was proposed to expose otherwise autoinhibited 2CARD (Kowalinski et al., 2011), but our MALS data (Figure S6A) and protease-protection assay (Figure 7A) suggest that, in addition to simple RNA binding, filament formation and additional conformational rearrangement during ATP hydrolysis are required for efficient oligomerization of 2CARD. Interestingly, our previous study showed that ATP hydrolysis also promotes filament disassembly, but not every ATP hydrolysis triggers MDA5 dissociation, especially on long dsRNA due to stabilization by the filament architecture (Peisley et al., 2011). We propose that the MDA5 filament provides a platform not only to bring individual 2CARD into proximity but also to allow formation and stable maintenance of 2CARD oligomers by supporting ATP hydrolysis decoupled from dissociation. The insufficiency of RNA binding and requirement of ATP hydrolysis and 2CARD oligomerization for MAVS activation are also shared with RIG-I, which appears to utilize K63-linked polyubiquitin, instead of filament formation, for 2CARD oligomerization (Jiang et al., 2012). Future research is needed to understand the precise nature of the dynamic coupling of 2CARD oligomers to the MDA5 filament during ATP hydrolysis and the mechanism that promotes MAVS filament formation.

EXPERIMENTAL PROCEDURES

Detailed experimental procedures are provided in the Extended Experimental Procedures online.

Crystallization and Structure Determination

The MDA5ΔN':dsRNA complex was assembled by mixing MDA5ΔN' (~1.5 mg/ml) and 12 bp RNA (Dharmacon) at a 2:1 molar ratio and was concentrated to ~10 mg/ml in buffer A (20 mM HEPES, pH 7.5, 150 mM NaCl, and 2 mM DTT) with 2 mM ADPNP. Crystals were initially obtained as small needles with the hanging-drop vapor-diffusion method from a 2:1 mixture of sample and reservoir buffer that contains 0.1 M MES (pH 6.5), 25% PEG300. Crystals were optimized with reservoir buffer containing 0.1 M MES (pH 7.0), 30% PEG300, and 7%–11% sucrose and using the micro-seeding method. Diffraction data were collected at NE-CAT beamline 24ID-C at the Advanced Photon Source and processed using the program XDS (Kabsch, 2010). The structure was determined by molecular replacement with Phaser (McCoy et al., 2007) and refined with Phenix (Adams et al., 2010) (see the Extended Experimental Procedures). A summary of data collection and structure refinement statistics is provided in Table S1.

Protein X-Linking and Mass Spectrometry

The four surface-exposed Cys's in MDA5ΔN' (residues 496, 536, 860, and 951) were mutated into Ala's, and a new Cys was introduced at position 556, 559, or 563. The complex of MDA5ΔN' and dsRNA was formed by mixing protein (200 nM) and dsRNA (12 μM 15 bp or 50 nM 112 bp) in buffer A at 37°C for 5 min. High concentration of 15 bp was used to compensate for the low affinity of MDA5 for 15 bp in comparison to 112 bp (Peisley et al., 2011). Protein X-linking was performed with 50 μM BMOE or sulfo-MBS (Pierce) at room temperature (RT) for 10 min and quenched with 50 mM DTT for BMOE or 25 mM DTT and 0.25 M Tris for sulfo-MBS prior to gel analysis and mass spectrometry (Extended Experimental Procedures).

MAVS CARD Filament Formation and Extension Assays

Refolded CARD-S was labeled with Alexa 488-benzylguanine (NEB) according to the manufacturer's instruction and further purified by SEC to remove unincorporated dye. Filament formation assay was performed by incubating monomeric, labeled CARD-S (CARD-S*) with 2CARD of RIG-I or MDA5 in buffer A for 2 hr at RT prior to analysis by Bis-Tris native PAGE (Life). Filament extension assay was performed by mixing unlabeled seed filaments and monomeric CARD-S* in buffer A for 30 min at RT prior to gel analysis. Fluorescent gel images were recorded using the scanner FLA9000 (Fuji).

ACCESSION NUMBERS

The PDB accession code for coordinates and structure factors is 4GL2.

SUPPLEMENTAL INFORMATION

Supplemental Information includes Extended Experimental Procedures, six figures, and one table and can be found with this article online at http://dx.doi.org/10.1016/j.cell.2012.11.048.

ACKNOWLEDGMENTS

The authors thank the NE-CAT beamline scientists for their assistance during data collection. F.C. acknowledges NIFA/USDA H00567 and UNH Karabelis Fund. T.W. is an Investigator in the Howard Hughes Medical Institute. S.H. is the recipient of a Pew Scholarship.

Received: August 14, 2012
Revised: October 12, 2012
Accepted: November 20, 2012
Published: December 27, 2012

REFERENCES

Adams, P.D., Afonine, P.V., Bunkóczi, G., Chen, V.B., Davis, I.W., Echols, N., Headd, J.J., Hung, L.-W., Kapral, G.J., Grosse-Kunstleve, R.W., et al. (2010). PHENIX: a comprehensive Python-based system for macromolecular structure solution. Acta Crystallogr. D Biol. Crystallogr. *66*, 213–221.

Baum, A., Sachidanandam, R., and García-Sastre, A. (2010). Preference of RIG-I for short viral RNA molecules in infected cells revealed by next-generation sequencing. Proc. Natl. Acad. Sci. USA *107*, 16303–16308.

Berke, I.C., and Modis, Y. (2012). MDA5 cooperatively forms dimers and ATP-sensitive filaments upon binding double-stranded RNA. EMBO J. *31*, 1714–1726.

Berke, I.C., Yu, X., Modis, Y., and Egelman, E.H. (2012). MDA5 assembles into a polar helical filament on dsRNA. Proc. Natl. Acad. Sci. USA *109*, 18437–18441.

Binder, M., Eberle, F., Seitz, S., Mücke, N., Hüber, C.M., Kiani, N., Kaderali, L., Lohmann, V., Dalpke, A., and Bartenschlager, R. (2011). Molecular mechanism of signal perception and integration by the innate immune sensor retinoic acid-inducible gene-I (RIG-I). J. Biol. Chem. *286*, 27278–27287.

Cui, S., Eisenächer, K., Kirchhofer, A., Brzózka, K., Lammens, A., Lammens, K., Fujita, T., Conzelmann, K.K., Krug, A., and Hopfner, K.P. (2008). The C-terminal regulatory domain is the RNA 5′-triphosphate sensor of RIG-I. Mol. Cell *29*, 169–179.

Ferrao, R., and Wu, H. (2012). Helical assembly in the death domain (DD) superfamily. Curr. Opin. Struct. Biol. *22*, 241–247.

Hou, F., Sun, L., Zheng, H., Skaug, B., Jiang, Q.X., and Chen, Z.J. (2011). MAVS forms functional prion-like aggregates to activate and propagate antiviral innate immune response. Cell *146*, 448–461.

Jiang, F., Ramanathan, A., Miller, M.T., Tang, G.-Q., Gale, M., Jr., Patel, S.S., and Marcotrigiano, J. (2011). Structural basis of RNA recognition and activation by innate immune receptor RIG-I. Nature *479*, 423–427.

Jiang, X., Kinch, L.N., Brautigam, C.A., Chen, X., Du, F., Grishin, N.V., and Chen, Z.J. (2012). Ubiquitin-induced oligomerization of the RNA sensors RIG-I and MDA5 activates antiviral innate immune response. Immunity *36*, 959–973.

Kabsch, W. (2010). XDS. Acta Crystallogr. D Biol. Crystallogr. *66*, 125–132.

Kato, H., Takahasi, K., and Fujita, T. (2011). RIG-I-like receptors: cytoplasmic sensors for non-self RNA. Immunol. Rev. *243*, 91–98.

Kowalinski, E., Lunardi, T., McCarthy, A.A., Louber, J., Brunel, J., Grigorov, B., Gerlier, D., and Cusack, S. (2011). Structural basis for the activation of innate immune pattern-recognition receptor RIG-I by viral RNA. Cell *147*, 423–435.

Li, X., Lu, C., Stewart, M., Xu, H., Strong, R.K., Igumenova, T., and Li, P. (2009). Structural basis of double-stranded RNA recognition by the RIG-I like receptor MDA5. Arch. Biochem. Biophys. *488*, 23–33.

Lu, C., Xu, H., Ranjith-Kumar, C.T., Brooks, M.T., Hou, T.Y., Hu, F., Herr, A.B., Strong, R.K., Kao, C.C., and Li, P. (2010). The structural basis of 5′ triphosphate double-stranded RNA recognition by RIG-I C-terminal domain. Structure *18*, 1032–1043.

Luo, D., Ding, S.C., Vela, A., Kohlway, A., Lindenbach, B.D., and Pyle, A.M. (2011). Structural insights into RNA recognition by RIG-I. Cell *147*, 409–422.

McCoy, A.J., Grosse-Kunstleve, R.W., Adams, P.D., Winn, M.D., Storoni, L.C., and Read, R.J. (2007). Phaser crystallographic software. J. Appl. Cryst. *40*, 658–674.

Myong, S., Cui, S., Cornish, P.V., Kirchhofer, A., Gack, M.U., Jung, J.U., Hopfner, K.-P., and Ha, T. (2009). Cytosolic viral sensor RIG-I is a 5′-triphosphate-dependent translocase on double-stranded RNA. Science *323*, 1070–1074.

Palsson-McDermott, E.M., and O'Neill, L.A. (2007). Building an immune system from nine domains. Biochem. Soc. Trans. *35*, 1437–1444.

Peisley, A., Lin, C., Wu, B., Orme-Johnson, M., Liu, M., Walz, T., and Hur, S. (2011). Cooperative assembly and dynamic disassembly of MDA5 filaments for viral dsRNA recognition. Proc. Natl. Acad. Sci. USA *108*, 21010–21015.

Peisley, A., Jo, M.H., Lin, C., Wu, B., Orme-Johnson, M., Walz, T., Hohng, S., and Hur, S. (2012). Kinetic mechanism for viral dsRNA length discrimination by MDA5 filaments. Proc. Natl. Acad. Sci. USA *109*, E3340–E3349.

Schlee, M., Roth, A., Hornung, V., Hagmann, C.A., Wimmenauer, V., Barchet, W., Coch, C., Janke, M., Mihailovic, A., Wardle, G., et al. (2009). Recognition of 5′ triphosphate by RIG-I helicase requires short blunt double-stranded RNA as contained in panhandle of negative-strand virus. Immunity *31*, 25–34.

Takahasi, K., Yoneyama, M., Nishihori, T., Hirai, R., Kumeta, H., Narita, R., Gale, M., Jr., Inagaki, F., and Fujita, T. (2008). Nonself RNA-sensing mechanism of RIG-I helicase and activation of antiviral immune responses. Mol. Cell *29*, 428–440.

Takahasi, K., Kumeta, H., Tsuduki, N., Narita, R., Shigemoto, T., Hirai, R., Yoneyama, M., Horiuchi, M., Ogura, K., Fujita, T., and Inagaki, F. (2009). Solution structures of cytosolic RNA sensor MDA5 and LGP2 C-terminal domains: identification of the RNA recognition loop in RIG-I-like receptors. J. Biol. Chem. *284*, 17465–17474.

Triantafilou, K., Vakakis, E., Kar, S., Richer, E., Evans, G.L., and Triantafilou, M. (2012). Visualisation of direct interaction of MDA5 and the dsRNA replicative intermediate form of positive strand RNA viruses. J. Cell Sci.

Wang, Y., Ludwig, J., Schuberth, C., Goldeck, M., Schlee, M., Li, H., Juranek, S., Sheng, G., Micura, R., Tuschl, T., et al. (2010). Structural and functional insights into 5′-ppp RNA pattern recognition by the innate immune receptor RIG-I. Nat. Struct. Mol. Biol. *17*, 781–787.

Yoneyama, M., Kikuchi, M., Matsumoto, K., Imaizumi, T., Miyagishi, M., Taira, K., Foy, E., Loo, Y.M., Gale, M., Jr., Akira, S., et al. (2005). Shared and unique functions of the DExD/H-box helicases RIG-I, MDA5, and LGP2 in antiviral innate immunity. J. Immunol. *175*, 2851–2858.